ELSEVIER

Contents lists available at ScienceDirect

Journal of Alloys and Compounds

journal homepage: www.elsevier.com/locate/jalcom



Lamellar instabilities during scanning laser melting of Al–Cu eutectic and hypoeutectic thin films



E.J. Sullivan^{a,*}, J.A. Tomko^a, J.M. Skelton^a, J.M. Fitz-Gerald^a, P.E. Hopkins^{a,b,c}, J.A. Floro^a

- ^a Department of Materials Science and Engineering, University of Virginia, Charlottesville, VA 22904, USA
- ^b Department of Mechanical and Aerospace Engineering, University of Virginia, Charlottesville, VA 22904, USA
- ^c Department of Physics, University of Virginia, Charlottesville, VA 22904, USA

ARTICLE INFO

Article history: Received 6 September 2020 Received in revised form 15 January 2021 Accepted 17 January 2021 Available online 19 January 2021

Keywords:
Metals and alloys
Nanostructured materials
Thin films
Laser processing
Microstructure
Phase transitions

ABSTRACT

Scanning laser melting was employed to investigate directional solidification in Al–Cu thin films, 200 and 500 nm thick. The Al–Cu alloy films, with both eutectic and hypoeutectic compositions, were co-deposited on fused silica substrates by magnetron sputtering. Melting of the films was carried out in air using a CW laser, as a function of the scan velocity, v, up to 5 cm/s. For eutectic films, regular lamellar microstructure was observed over the entire range of velocities studied. Interlamellar spacings, λ , below 50 nm were readily produced. Results were found to be consistent with studies on bulk Al–Cu alloys, obeying the classic steady state lamellar growth relationship, $\lambda^2 v = K$. However, the value of the constant, K is significantly larger in thin films when compared to bulk. This is attributed to constraints on mechanisms for spacing adjustment in two-dimensional eutectic systems. In the hypoeutectic thin films, a complex lamellar structure was observed as the scan velocity was reduced. Regions of straight lamellae, oscillatory lamellae, solitary tilt waves, and recurring extreme lamellar branching events coexisted across the melt track. Fourier analysis was used to quantify the chaotic area fraction of the films. The transition to chaos occurred as the G/v ratio increased, attributed to approaching a re-entrant eutectic-to-dendritic transition from above. Approaches to further refine laser melting in thin eutectic films in order to better control solidification processes are discussed

© 2021 Published by Elsevier B.V.

1. Introduction

Controlling heat flow during the solidification of a eutectic alloy allows for direct control of microstructural length scales and morphology. Electrical, mechanical, magnetic, and thermal properties can be significantly modified by the periodicity of these features. Typical eutectic microstructures can be categorized as irregular or regular, with the latter having either a lamellar or rod-like structure depending on volume fraction of each constituent phase, where, for example, lamellar spacings down to the 10¹ nm scale have been obtained in the Al–Cu system [1]. Eutectic solidification has been investigated extensively in the context of mechanical properties [2] and is now the subject of investigation in the context of additive manufacturing of metals [3,4]. In addition, eutectic solidification provides a relatively unexplored processing approach for nanocomposite materials and applications including exchange-coupled ferromagnetism, thermoelectrics, [5,6] and photovoltaics. The ability

* Corresponding author. E-mail address: eks9fa@virginia.edu (E.J. Sullivan).

to dictate the lengthscales of the interleaved eutectic microstructure are relevant, for example, in controlling scattering of thermal and electronic carriers, or determining the extent of magnetic exchange interactions [7,8]. Of course, there is a strict limitation to this approach since material systems of relevance must be identified which feature a useful eutectic point in the binary or ternary phase diagram. Applications such as these often involve the use of thin films, where less information exists on the behavior of eutectic solidification. In addition, thin films are of fundamental interest in that they offer new opportunities to examine the effect of fine-scale dimensional constraints on the eutectic length scale and can provide insight regarding how periodic perturbations affect the propagating solidification front. These opportunities would take advantage of the well-established approaches to patterning thin films with lithography and masked depositions, at lengthscales from tens of micrometers down to tens of nanometers.

To lay the groundwork for exploring eutectic solidification in more complex thin film systems, fundamental aspects of directional hypo/eutectic solidification in metallic systems were first investigated with Al–Cu films less than 1 µm thick. While some work

has already been done on metallic films [9–12] the vast majority of experiments in metals have focused on bulk samples. In this paper, the effects of scanning laser melting and subsequent solidification of Al-Cu thin films with both eutectic and hypoeutectic compositions were investigated. Directional solidification via scanning laser melting allows straightforward control over the solidification velocity at speeds from 10^{-2} – 10^{2} cm/s. However, the peak temperature and the thermal gradient are not controlled nor easy to determine in laser-based experiments, and the macroscopic melt boundary will have non-zero curvature, leading to lamellar bending over extended lengthscales. This paper offers two primary scientific emphases. The first emphasis establishes the regularity of the solidification behavior in films at the eutectic composition. This model system has been thoroughly studied throughout the years [1,13-21]. Regular, coupled, lamellar growth is well known in the Al-17.1 at% Cu eutectic system, including in films of order several micrometers in thickness [13]. In this work, it is shown that eutectic thin film (200–500 nm thick) samples follow the usual relationship, $\lambda^2 v = K$ derived by Jackson and Hunt, where λ is the interlamellar spacing (ideally measured at the minimum undercooling, but more typically just an average value from micrographs), v is the solidification velocity, and the constant K depends on the alloy system [22]. However, the value of K is found to be significantly larger in thin films than that for the equivalent bulk alloys, and is line with values obtained in previous micron-thick film work [13]. This is attributed to the two-dimensional (2D) nature of films and lack of spacing adjustment mechanisms that threedimensional (3D) systems possess, such as lamellar faults. Having established the behavior of eutectic thin films, the second emphasis is on instabilities in hypoeutectic thin films. The simplified 2D imaging geometry is useful in order to examine instabilities during solidification, and a rich literature exists in this area for transparent organic eutectics [23-25]. In this work, hypoeutectic Al-Cu thin films are shown to exhibit standard instability modes observed in both bulk Al-Cu [26] and organic eutectics. It is shown here that Al-Cu hypoeutectic films also exhibit highly non-linear instabilities consisting of interacting oscillatory instability modes, solitary tilt waves, and recurring extreme lamellar branching. The formation of these structures is found to depend on the reduced spacing Λ , and these structures become more prevalent as the G/v ratio (the ratio of the thermal gradient to the solidification velocity) increases. It is hypothesized that the extreme lamellar branching events are due to a re-entrant approach to dendritic growth, consistent with behavior reported in Al-Cu solidification microstructure selection maps.

2. Material and methods

Al-Cu films were co-deposited using a high vacuum, direct current magnetron sputtering system with a base pressure of 5.0×10^{-8} Torr. Elemental Al and Cu targets 3" in diameter (purity ≥ 99.9%) were used for the experiments. Ultrahigh purity Ar was used as the sputter gas, maintained at a pressure of 1 mTorr during deposition. The films were deposited at room temperature, while the substrate rotated at 8 RPM. Fused silica substrates were used in all experiments with a single-side polish (JGS2 type, 20 mm × 20 mm x 1 mm) and a roughness of < 5 nm. Fused silica was chosen due to its low thermal conductivity (about 1 W/m-K), so that heat extraction would primarily occur through the film and not the substrate, thus allowing for temperature rises in the metal film from laser absorption [27] that are high enough to induce melting using readily available laser systems [28]. Prior to deposition, the substrate was rinsed in deionized (DI) water, ultrasonciated in acetone for 10 min, rinsed again in DI water, ultrasonciated in isopropyl alcohol for 10 min, rinsed in running DI water for 2 min, and then dried with bursts of N2 gas.

Film composition was controlled by the power to the Al and Cu sputter targets. Calibration of the relative powers was achieved

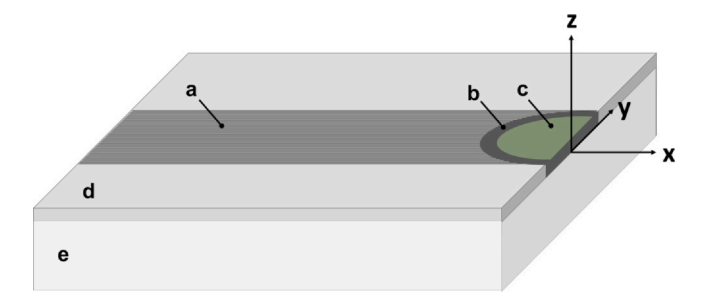


Fig. 1. Schematic of the film laser irradiation experiments: a – resolidified film, b – melt pool, c – laser spot, d – as-deposited film, and e – substrate. The laser scan direction is parallel to x, y is the transverse direction, and z is normal to the film plane. The relative feature dimensions are not to scale.

through film thickness measurements obtained by weighing; the duration of deposition was varied, and the mass of the deposited film was measured with a balance to an accuracy of 0.01 mg. Given a known area of the substrate (typically a 3" diameter wafer), and assuming bulk density (valid for low melting point metals), deposition rates were calculated and 200 and 500 nm thick films were grown. Two film compositions will be discussed; the first is nominally at the eutectic composition while the second was deliberately deposited at a hypoeutectic composition.

The alloy films were melted in air ambient using a Spectra-Physics Millennia eV CW solid-state laser, operating at 532 nm with a 5 W maximum power. The circular beam was spread using a cylindrical lens to form an ellipsoidal spot, with the long axis orthogonal (along y in Fig. 1) to the direction of laser scan (along x in Fig. 1). The final laser spot had a $1/e^2$ beam width of 180 μ m by 100 μ m in diameter from a Gaussian fit using a scanning-slit beam profiler. For a laser power of 5 W, an incident power density of order 3.5×10^5 kW/m² could be obtained. The sample was secured to a Newport M-ILS50PP translation stage, which provided a range of scan speeds from 0.001 to 5 cm/s, and translated under a stationary beam, which maintained normal incidence of the laser to the film. Given that the substrate diameter was of order 200 times larger than the width of a melt track, all experimental melting runs could be performed on a single film with a given composition and thickness.

After melting, backscattered electron (BSE) imaging was performed on the film's surface, defined as the x-y plane in Fig. 1, using a FEI Quanta 650 SEM. As θ contains more Cu, the brighter lamellae correspond to the θ phase and the darker lamellae are the α phase. To examine the lamellar morphology in the z-direction, 10 μ m wide cross sections (y-z plane in Fig. 1) were milled using a FEI Helios DualBeam Focused Ion Beam (FIB). These were obtained from the central regions of the melt track (see Fig. S1 in Supplementary materials).

Micrographs were processed using the open source ImageJ software package to obtain measurements of phase area fractions and interlamellar spacing measurements, and to further analyze the chaotic behavior discovered in the hypoeutectic samples.

To determine the area fractions of each phase, BSE micrographs were imported into ImageJ and thresholding was applied to create a binary image, by which a direct measurement was made for the area fractions of α and θ , based on Z-contrast. Local interlamellar spacing distributions, $\lambda(y)$, were measured on BSE micrographs by counting the number of lamellae intercepting an orthogonal line of known length, typically spanning of order 50 lamellae. The lamellae are assumed to be uniform in the direction normal to the image, which was verified in select samples using FIB cross-sectioning. The average interlamellar spacing over extended areas was obtained by applying a 2-D Fast Fourier Transformation (FFT) to the micrographs (see Fig. 2). Two prominent peaks in the Fourier power spectral density are observed. The line connecting these peaks is perpendicular to the average lamellar direction. We will refer to these as

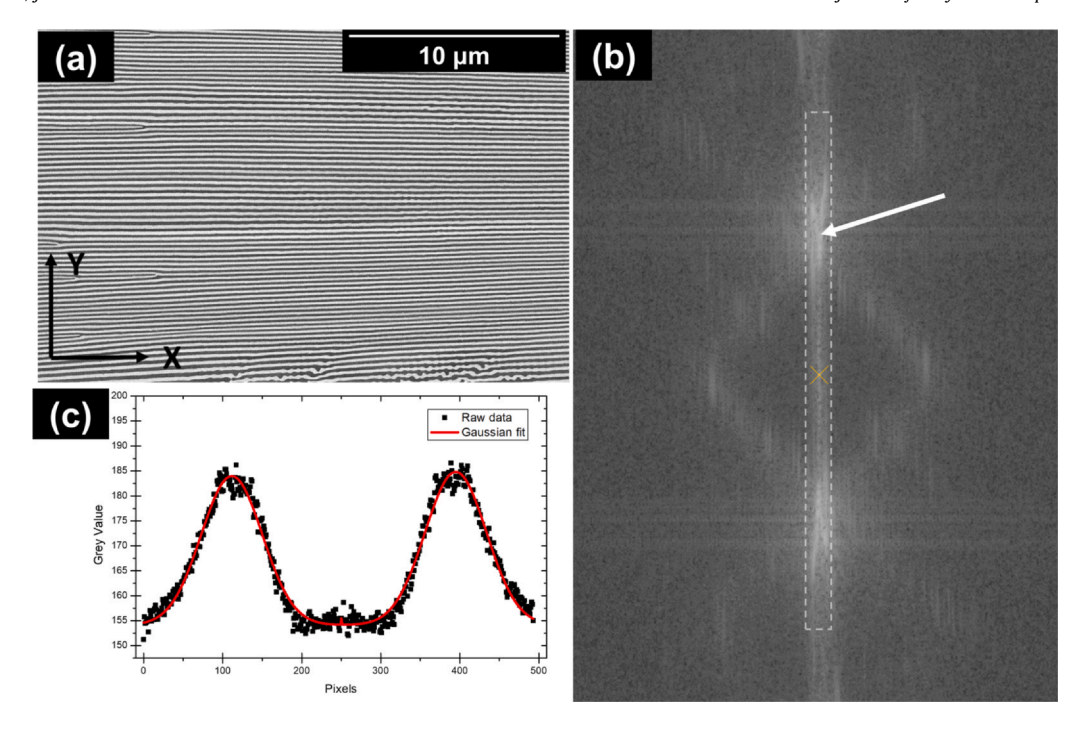


Fig. 2. Example of an interlamellar spacing measurement using FFT. (a) BSE micrograph of a 200 nm thick, eutectic film resolidified at 5 W and 0.2 cm/s, from left to right; (b) FFT of (a), where the center of the FFT is indicated by a yellow X and the first diffraction peak is indicated by the white arrow; and (c) is the integrated intensity profile along the rectangular selection in (b).

lamellar diffraction peaks. The peak position can give the mean lamellar spacing as $\lambda_{\rm av} = |{\bf k}_{\rm max}|^{-1}$, once the calibration of image distances is established from the image magnification. The peak position, $|{\bf k}_{\rm max}|$, is obtained from a rectangular selection that integrates intensities in the direction normal to ${\bf k}_{\rm max}$, and the resulting intensity profile was fit using a Gaussian function. The average interlamellar spacing obtained from linear intercepts were in close agreement with the FFT results.

Fourier analysis was also used to quantify the area fractions of chaotic and highly-bent lamellae in the hypoeutectic samples (see Fig. 3). Regions containing tortuous lamellae are associated with frequencies in reciprocal space not included in the primary lamellar diffraction peaks. Preferred lamellar tilt directions lead to additional intensity arcs while solitary tilt waves [29] lead to formation of streaks; both features are indicated in Fig. 3b. A mask was created to only pass the intensity from the lamellar diffraction peak in the Fourier space image. Using this mask, an inverse-FFT was applied to recreate a real space image formed only from the pass frequencies. The resulting real space image was then thresholded to form a binary image, see Fig. 3c. In this image, the area fraction of the image containing black pixels includes both the excluded frequencies, associated with chaotic lamellae, as well as the lamellae from the α phase in the regions with parallel lamellae. It is readily shown that the area fraction of the chaotic regions only, F_c, can be obtained by $F_c = (F_{bl} - F_{\alpha})/(1 - F_{\alpha})$, where F_{bl} is the area fraction of black pixels, and F_{α} is the area fraction of the α lamellae, measured in adjacent regions containing parallel lamellae.

Standard-less energy dispersive x-ray spectroscopy (EDS) measurements, both area and line scans, were obtained in the SEM. In general, the absolute accuracy is not considered to be reliable, but the relative compositions of different specimens having the same film thickness should be meaningful. These EDS measurements indicate that the hypoeutectic film contained about 3 at% less Cu than the nominal eutectic film (see Fig. S2). Measured area fractions of the hypoeutectic film determined that θ made up 42.7 \pm 0.5% of the surface, which corresponds to 15.3–15.6 at% Cu. Subsequently, the hypoeutectic film will be assumed to be approximately 14–15 at% Cu.

3. Results

For this investigation, it is adopted that the resultant phases are the equilibrium α and θ phases, since the conditions herein are far from a true rapid solidification regime where variants on the θ phase might form [1,30]. Phase identification using x-ray diffraction could not be performed, as the transformed volume associated with relatively narrow melt tracks in thin films yields too little signal. From the contrast in BSE-SEM, and resultant EDS, a melt track contains alternating phases that contain different Cu concentrations, which nominally correspond to α and θ , and these lamellar phases have compositions that are different than the mean composition of the surrounding film. EDS linescans also indicated that the composition was consistent across the melt track; there was no observable macrosegregation of Al or Cu in the melt pool.

Nominally eutectic composition Al–Cu films were investigated first to verify that well-characterized relationships for the dependence of lamellar spacing on the velocity of the solid/liquid interface are retained in very thin films. This also helps when interpreting behavior observed in hypoeutectic films described after. Laser melting scans of varying scan speeds and powers were performed on the same film, so resultant eutectic structure and melt track width could be directly compared at identical composition and film thickness.

3.1. Eutectic films

In the eutectic films, all laser melting experiments resulted in lamellar structure. The range of laser scan speeds, v, where melting took place was from 0.01 cm/s to 5.0 cm/s. Across this range of velocities, the laser output power was held constant at 5 W, hence the effective fluence (incident optical energy/area) varied inversely with v. As a result, for the 200 nm thick films, at any v < 0.01 cm/s, the films would overheat and ablate and/or spall, revealing a fractured substrate interface region, indicative of thermal shock. For scan speeds > 3.0 cm/s, melting did not occur. For the 500 nm thick film, melting was observed up to and including 5.0 cm/s while processing

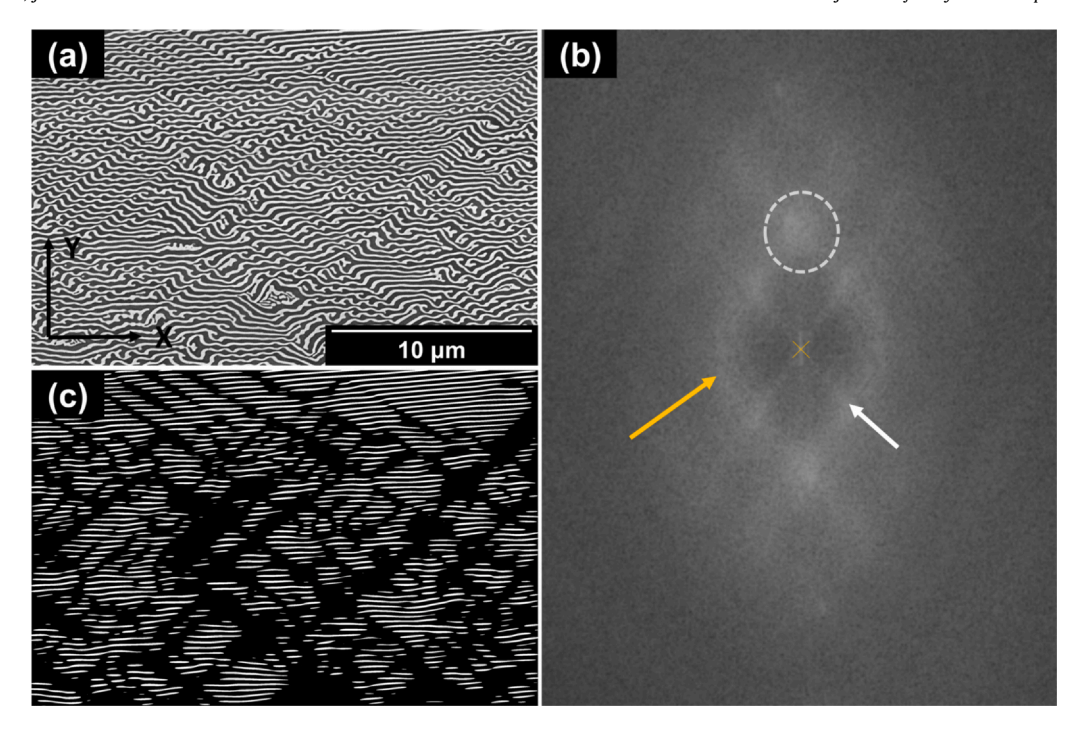


Fig. 3. Example of measurement of the chaotic lamellar area fraction. (a) BSE micrograph from a 200 nm thick, hypoeutectic film resolidified at 5 W and 0.2 cm/s; (b) FFT of (a), where the center is indicated by a yellow X, the first diffraction peak is circled, the yellow arrow indicates the arcs associated with chaotic lamellae, and the white arrow points along the streak associated with solitary tilt waves; (c) is the inverse FFT of the same region as (a) with only the frequencies inside of the dotted circle in (b) passed., i.e. excluding the streaks associated with chaos, and the gray scale is binary. (For interpretation of the references to color in this figure legend, the reader is referred to the web version of this article.)

using a higher optical power density. Cross sections prepared using the FIB on the 200 nm thick film confirmed that the film melted through the entire thickness, with lamellae oriented perpendicularly to the substrate and homogeneously spanning the entire film thickness.

Fig. 4 shows typical micrographs of melt tracks on 500 nm thick films for two laser scan speeds. The edges of the melt track are linear and bounded by a heat-affected zone (HAZ) of constant width at a

given scan speed. The HAZ exhibits coarsened two-phase structure on either side of the melt, and its width is always much smaller than the molten track. In Fig. 4, the solidification fronts may be crudely traced. In a system with purely isotropic interfacial energies, lamellae will act like streamlines, aligned perpendicular to the locally advancing liquid/solid interface. The continuous curvature of lamellae from the HAZ to the center of the melt then indicates the shape of the *macroscopic* solid-liquid interface growth direction, or

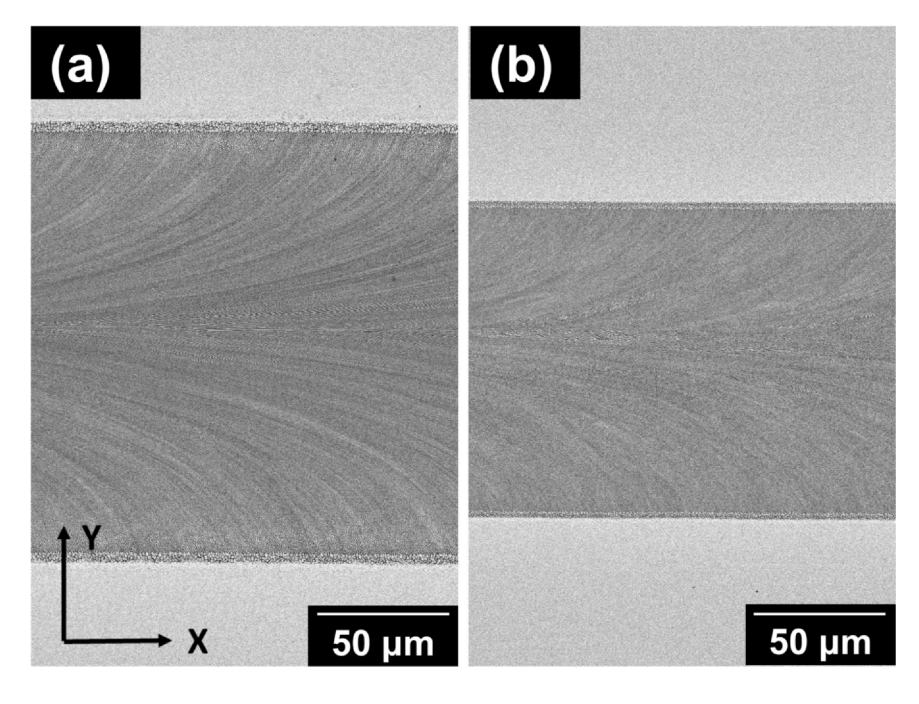


Fig. 4. BSE micrographs from 500 nm thick, eutectic film laser melted from right to left at 5 W. The darker regions are melted and resolidified, and the striations are from the nanoscale eutectic. The surrounding film (light gray) was not melted. Scan speeds were (a) 0.2 cm/s and (b) 1.0 cm/s.

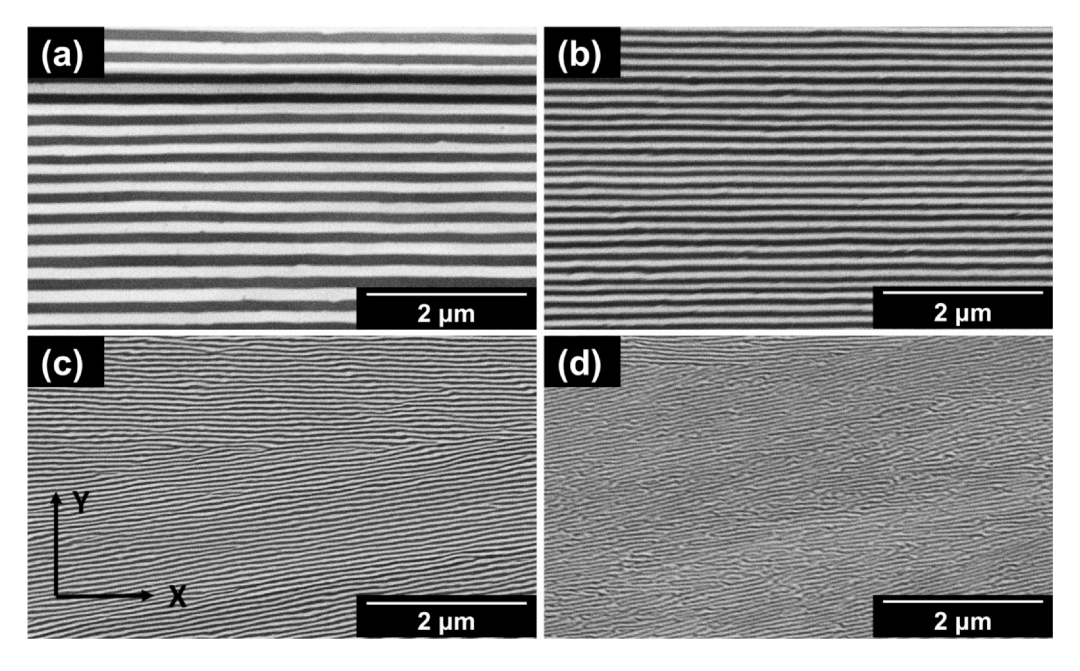


Fig. 5. BSE micrographs from 200 nm thick, eutectic films resolidified at 5 W and: (a) 0.1 cm/s, λ_{av} = 290 nm; (b) 0.5 cm/s, λ_{av} = 153 nm; (c) 2.0 cm/s, λ_{av} = 74 nm; and (d) 3.0 cm/s, λ_{av} = 64 nm.

equivalently, the direction of heat extraction during solidification. The strong curvature of the lamellae shows that heat conduction through the adjacent unmelted film is significant, such that only the center of the melt zone solidifies parallel to the laser scan direction.

Fig. 5 shows characteristic solidification structures in 200 nm thick eutectic films, across a range of scan speeds. The lamellae in the central region of the track are linear and correlated over large distances both in the transverse and longitudinal directions for $v \le 0.5$ cm/s. For v > 1 cm/s, lamellar waviness becomes apparent, and, in lower magnification images, grain boundaries become apparent. At higher velocities, the grain size decreases, and the lamellar directions become locally more divergent between adjacent grains. This waviness is not correlated, e.g., they are not in the form of periodic oscillations such as the $1\lambda O$ and $2\lambda O$ morphologies that are frequently observed in organic eutectics [24,25] and also in Al–Cu [26]. In rare instances, such oscillations were observed in the eutectic films, and the implications of this, as well as the uncorrelated waviness, will be discussed later. Across the range of velocities studied here, λ decreased with increasing velocity, as expected.

3.2. Hypoeutectic films

A 200 nm thick, hypoeutectic film was investigated using an abbreviated range of laser scan velocities from 0.2 to 1.0 cm/s, where each scan speed was performed at laser powers of 4 W and 5 W. As with the eutectic film, the energy absorbed for each melt track differed, and consequently the thermal gradient G and thus G/v differed for each run (see the Discussion, and Fig. S3 in Supplementary materials).

Fig. 6 depicts the melt tracks, where, as expected, increasing the scan velocity at a constant power resulted in narrower tracks. Bordering the melt track is a partially melted zone (PMZ), wherein the temperature surpassed the eutectic temperature but not the liquidus temperature, $T_L(C)$, C being the hypoeutectic film composition. As a result, this region contains coarsened, unmelted α islands, and in regions where the inter-island separation exceeds the local diffusion length, eutectic lamellae grow in-between the islands. In the central track region between the PMZ's, $T(y) > T_L(C)$, and full melting occurs. Right along the boundary where $T \approx T_L$, some coarsened α grows dendritically into the melt for a short distance before being occluded

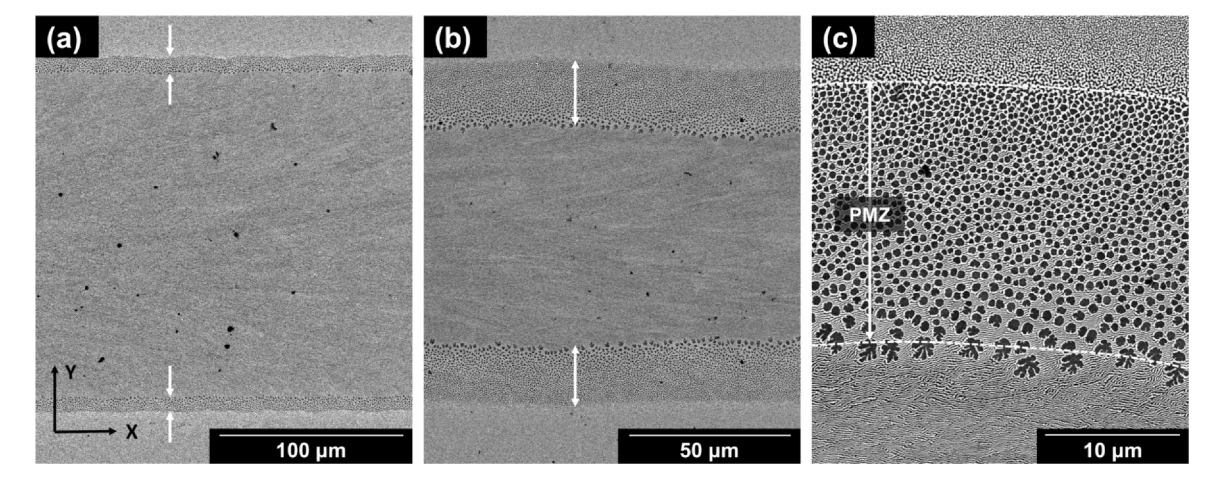


Fig. 6. BSE micrographs showing melt tracks of a 200 nm thick, hypoeutectic film solidified from right to left at 4 W and (a) 0.2 cm/s and (b) 1.0 cm/s. Note the difference in magnification. White arrows denote the partially melted zone (PMZ). (c) Magnified region of the PMZ on the top of the track in (b). The black specks seen on the surface are residual contamination that was not present during the melting.

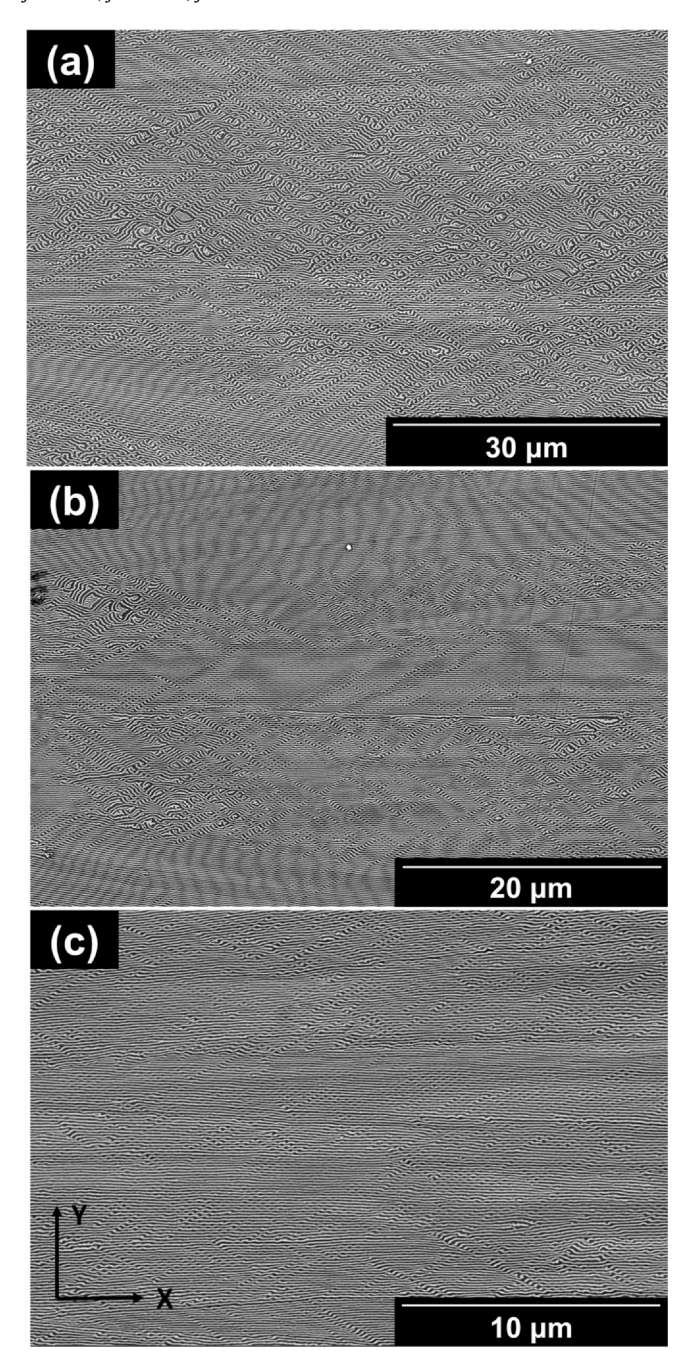


Fig. 7. BSE micrographs from the center of the melt track of a 200 nm thick, hypoeutectic film resolidified at 5 W at (a) 0.2 cm/s, (b) 0.5 cm/s, and (c) 1.0 cm/s.

by the more rapid lamellar growth. In the fully melted region of the track the lamellar microstructure contains a volume fraction of the α phase consistent with a hypoeutectic composition. In the hypoeutectic

experiments, small periodic fluctuations in laser power (< 1%) created a detectable periodic variation in the width of the track. The width of the PMZ was found to increase with velocity at constant laser power, and for velocities in excess of $2.0\,\mathrm{cm/s}$ (not shown here), the entire track is only partially melted (i.e., T never exceeds T_L). As with the eutectic films, at the edge of the track, heat is conducted to the surrounding film, so that eutectic grains nucleate at the edge of the track (really, the edge of the PMZ) and solidify inwards towards the center of the track, forming lamellae that curve from edge to center.

In the fully melted regions where coupled α/θ growth occurs, there are interesting variations in the lamellar morphologies (see Fig. 7). Results for 4W irradiation can be found in Fig. S4. Similar to the eutectic samples, λ decreased with increasing velocity. However, as opposed to the mostly parallel, regular lamellae exhibited in eutectic films at these solidification velocities, the hypoeutectic films contain regions of periodically oscillating lamellae, solitary tilt waves, and chaotic lamellae. These latter, more tortuous, regions occurred more frequently at the slower scan speeds. Table 1 summarizes the area fractions of chaotic lamellar regions, obtained using FFT bandpass filtering as described in Section 2. Notably, there is a rapid increase in the chaotic area fraction around 0.2 cm/s.

Fig. 8 further highlights the various morphologies that develop across the range of growth conditions. At the lowest scan velocity (v = 0.2 cm/s), a frequently observed structure is what we will call an extreme lamellar branching (ELB) event, highlighted by an arrow in Fig. 8a. In all cases it is the primary α phase that splits into two highly-tilted branches, and in many cases, there is subsequent growth of a new lamellar region inside the branches whose periodicity is much smaller than the surroundings. Many examples of this structure can also be seen upon close examination of Fig. 7a. ELB events were still present at 0.5 cm/s but less frequently, and none were observed for v = 1 cm/s. Hook-like features were observed at both 0.2 and 0.5 cm/s. Very few hooks were observed at 1 cm/s. Patches of oscillatory lamellae were present at all velocities, tending to increase in overall area fraction as the scan velocity increased. Regions of relatively straight lamellae existed even in the most chaotic samples. Overviews of the hypoeutectic melt tracks are included in the Supplementary materials (Fig. S5) that show the full morphological evolution from the PMZ boundary to track center.

4. Discussion

Scanning laser solidification in submicron Al–Cu thin films on fused silica substrates produces eutectic lamellar growth at the eutectic composition across a range of scan velocities. For hypoeutectic compositions, partially melted zones containing unmelted α and eutectic lamellae exist along the edge of fully melted regions, which can exhibit a more complex morphology. Here we discuss these results for eutectic and hypoeutectic thin films of Al–Cu, relative to well–known results in bulk Al–Cu. We will also make frequent comparisons to the results from experiments in transparent organic eutectic systems, especially $\text{CBr}_4\text{-C}_2\text{Cl}_6$. A deep understanding of the instability modes that occur when solidifying through the eutectic isotherm comes from the extraordinarily well–controlled and

Table 1Measured and derived quantities obtained from the melt tracks of a 200 nm thick, hypoeutectic film. The upper and lower bounds on average G_y (thermal gradient along y) and G_y (v correspond to 14 and 15 at% Cu, respectively.

-						
Laser Power [W]	Scan speed [cm/s]	Average lamellar spacing [nm]	Reduced lamellar spacing	Area fraction of chaotic lamellae [%]	G _y [/10 ⁶ K/m]	G _y /v [/10 ⁵ K*sec/cm ²]
5	0.2	277.3	1.35	55.7	3.6-5.6	1.81-3.73
	0.5	183.8	1.42	16.3	2.9-4.5	0.58-1.20
	1.0	115.4	1.26	15	1.8-2.8	0.18-0.37
4	0.2	270.0	1.32	20.8	2.0-3.1	1.01-2.09
	0.5	167.6	1.29	11.6	1.5-2.3	0.30-0.63
	1.0	113.0	1.23	12.4	0.8-1.2	0.08-0.16

Fig. 8. 200 nm thick, hypoeutectic film resolidified from right to left at 5 W and (a) 0.2 cm/s, (b) 0.5 cm/s, and (c) 1.0 cm/s. An extreme lamellar branching (ELB) event is indicated by the yellow arrow in (a), where other ELBs are present in the micrograph. A hook-like feature is indicated by the yellow arrow in (b), and numerous similar features are present. Inset in (b) includes white arrows that indicate solitary tilt waves converging, creating a possible proto-ELB event. (For interpretation of the references to color in this figure legend, the reader is referred to the web version of this article.)

analyzed experiments possible in this system; see, for example, a comprehensive account from Ginibre, et al. [24]. Additionally, we will draw significant insights from the work of Karma and Sarkissian (K-S) [25], who used a boundary integral approach to predict the appearance of different instability modes as a function of composition and local lamellar periodicity. Their modeling used parameters specific to the CBr₄-C₂Cl₆ system, as well as for a hypothetical system with a symmetric eutectic phase diagram. The K-S theory is strictly applicable in the quasistatic approximation, where the diffusion field can adjust rapidly in response to changes in the interfacial shape. This requires that the Peclet number, $P = \lambda v/2D$, be << 1, where D is the liquid phase diffusion coefficient. The hypoeutectic films herein have $P \approx 0.1$, at the upper limits of applicability. In addition, K-S used much smaller values of G and v, appropriate to the experiments with organic eutectics. Values for G and v here are both about 10³ times larger, such that the G/v ratio is similar. For the most part, our comparisons with these works will be qualitative, emphasizing similarities that can be ascribed to current understanding, and where they occur, differences in the behaviors in thin metallic films vis-à-vis the organics.

4.1. Eutectic results

Of key interest in eutectic systems is the relationship between the interlamellar spacing, λ , and the velocity of the solidification front, v. Fig. 9 plots λ (obtained by the FFT method) vs. v on log-log axes for both 200 nm and 500 nm thick films. The data are

superimposed upon a compendium of results from other workers, primarily obtained in bulk Al–Cu specimens [1,14–21]. Fig. 9 shows that for films down to 200 nm thickness, the eutectic solidification behavior is very similar to that observed in the bulk. Also shown in Fig. 9 are the results of Cline for directional solidification in Al–Cu eutectic films that were 2 μ m thick [13]. Cline noted that the magnitude of the periodicity in films tends to exceed that which was measured separately in bulk material over a similar range of velocities. Our data behaves similarly. For the data set represented in Fig. 9, separate fitting was performed to the bulk data vs. the thin film data (this work and Cline's) using the same expression. The fits yield $K_{\rm bulk}$ = 88.8 μ m³/s, whereas $K_{\rm film}$ = 119 μ m³/s.

The large difference between the measured values of $K_{\rm bulk}$ and $K_{\rm film}$ in Al–Cu can arise from two sources – actual differences in the values of the thermophysical parameters that make up K, or the way in which K is determined in experiments from measurements of λ . The theoretical form of the constant K, here labeled as $K_{\rm JH}$, is wellestablished from Jackson–Hunt theory, in the regime where the Peclet number is small [22]. Values of the thermophysical parameters for Al–Cu have been continuously refined over the years, leading to differing estimates for K. The most recent calculation, by Senninger, et al., in 2018, employs updated thermodynamic databases to predict $K_{\rm JH}$ = 90 μ m³/s at the eutectic composition [31]. This value also uses D = 2.4×10^{-9} m²/s, where D is the effective diffusion coefficient. The importance of this is discussed next. Note also that some solidification studies in the bulk Al–Cu eutectic system have produced larger values of K_{bulk} .

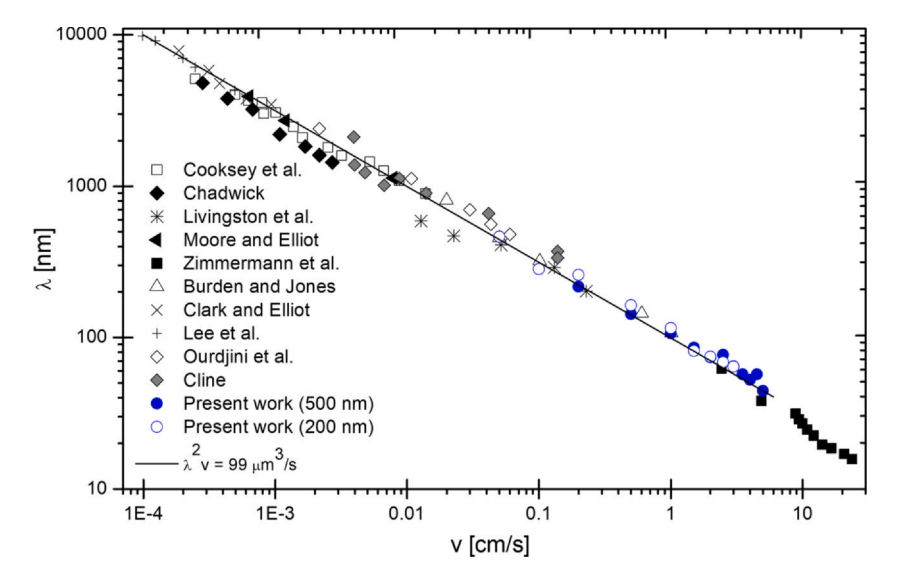


Fig. 9. Results obtained here for thin films, in blue, overlaid directly onto previously published work for the Al-Al₂Cu eutectic system [1,14–21]. The linear fit pictured here is for all data except for the rapid solidification regime from Zimmerman, et al.

It is not trivial to explain the large difference between the measured values for Al-Cu thin films vs. measured bulk values, and the predicted values, by manipulating the thermophysical parameters of K_{IH} [22]. It is unlikely to be a small-thickness (Gibbs-Thomson capillary) effect on the thermodynamic equilibria, even in the thinnest (200 nm) films examine here. The melting points of metallic nanoparticles, for example, only show significant depression for particle radii < 25 nm [32]. Furthermore, note that the fit to the thin film data in Fig. 9 includes films ranging up to 2 µm in thickness. The value of K does have an explicit composition dependence via the phase fractions [30]; however, the difference in K_{film} would require a hypoeutectic deviation in composition that is much larger than is possible in these experiments. Lastly, as discussed by Senninger, et al., the value of K_{IH} is directly proportional to the effective diffusion coefficient. For solidification geometries where convective mixing is significant, D values will be larger, leading to larger $K_{\rm IH}$. For example, Tassa and Hunt obtained $K = 127 \,\mu {\rm m}^3/{\rm s}$ for a situation where they report D = 3.6×10^{-9} m²/s [33]. Witusiewicz, et al., [34] obtained a fit value of 135 µm³/s, even larger than found here, where their fit relied heavily on data from Ourdjini, et al., [21] which may also result from convection effects increasing the effective diffusion coefficient. The value of D = 2.4×10^{-9} m²/s is typical of experiments in which convection is suppressed. In the thin films used here, convection is unlikely to play any role. Hence it is concluded that $K_{\text{film}} > K_{\text{IH}} \ge K_{\text{bulk}}$ is not explained by the diffusion coefficient [31].

Alternatively, the measured value of K can depend on how the lamellar periodicity is quantified. Here, as is often done, the periodicity is determined as an average value obtained from micrographs. Walker, et al., performed directional solidification experiments in Al-Cu in which the material was considered to be fully 3D since the transverse dimension, t, obeyed $t >> \lambda$ [35]. They suppressed convective currents in the melt that could muddle interpretation by melting in a microcapillary tube. They established that in the 3D case, the range of stable lamellar periods was $(1-1.2)\lambda_{min}$, and λ_{av} = 1.1 λ_{min} , where λ_{min} is the smallest stable spacing (nominally at the minimum undercooling) [36]. This is a much narrower range, and lower mean value, than what is found in organic thin films, such as those reported by Ginibre, et al. [24], where maximum wavelengths $\geq 2\lambda_{min}$ were observed. Walker, et al., argued that 3D systems have facile mechanisms for wavelength adjustment that 2D systems lack, specifically through the presence and action of lamellar faults [37].

For a select range of solidification speeds, the distribution of lamellar spacings were measured in 200 nm thick eutectic films, typically encompassing at least 40 lamellar pairs. If these distributions are normalized by the *minimum* observed value as $\Lambda = \lambda/\lambda_{min}$, then the distributions show an extended range (compared to Walker, et al.) of $\Lambda \sim 1$ –1.5, see Fig. S6. Hence, our determination of the value of K_{film} using average values of λ obtained from the FFT are likely skewed larger by a broadened distribution of lamellar periods in the films. The range of Λ is important to lamellar instabilities, which are discussed below. However, since the value of λ_{min} has not been obtained in every sample here, a proxy value, Λ_{JH} will be used, $\Lambda_{JH} = \lambda/\lambda_{JH}$, where λ_{JH} is the Senninger, et al., value of 90 $\mu m^3/s$.

There is no identifiable trend between our measured value of the mean normalized lamellar spacing $\langle \Lambda_{IH} \rangle$, obtained from FFT, and the geometrical "2D"-ness, represented by the ratio T = t/λ_{av} , where $T >> \lambda$ would nominally be 3D. For the eutectic films of thickness 200 and 500 nm studied here, over the full range of scan speeds, $0.7 \le T \le 10.2$. Cline's films are also in this range of T [13]. Fig. 10a shows that $<\Lambda_{IH}>\sim 1.1-1.3$, with no dependence on T, suggesting that all the films are behaving as 2D entities. A parameter that would have more value for defining 2D vs. 3D in the context of lamellar spacing adjustment would be the ratio of the film thickness to the lamellar fault spacing. While a systematic examination of transverse cross-sections was not performed, it seems likely that even in the thickest films, the presence of film free surface and interface with the substrate would alloy faults to rapidly grow out of the film as the solidification front propagates. Another consideration is that Walker, et al., noted a need to assure that the system is truly in steady state. This is an inherent limitation of a laser-based experiment, and this will be further commented on below.

Small regions of lamellar oscillations were observed in the eutectic films (see, for example, the lower portion of Fig. 2a). Based on their random locations along the track length, they are not specifically related to any small variations in the scan speed or laser power. Although the limited areas over which these oscillations occur in the eutectic films makes identification difficult, the oscillations are best assigned to the $1\lambda O$ mode [25]. This agrees with K-S, who predicted that when the alloy composition is close to the eutectic (and *only* when it is), $1\lambda O$ will be the first instability mode to manifest. Extended, essentially stable regimes of periodic oscillations occur when the reduced lamellar spacing, Λ , exceeds ~2. In the limited region in Fig. 2a, $\Lambda_{\rm JH}$ ~ 1.6, consistent with transient oscillations occurring in regions of locally larger spacing. The variation in the

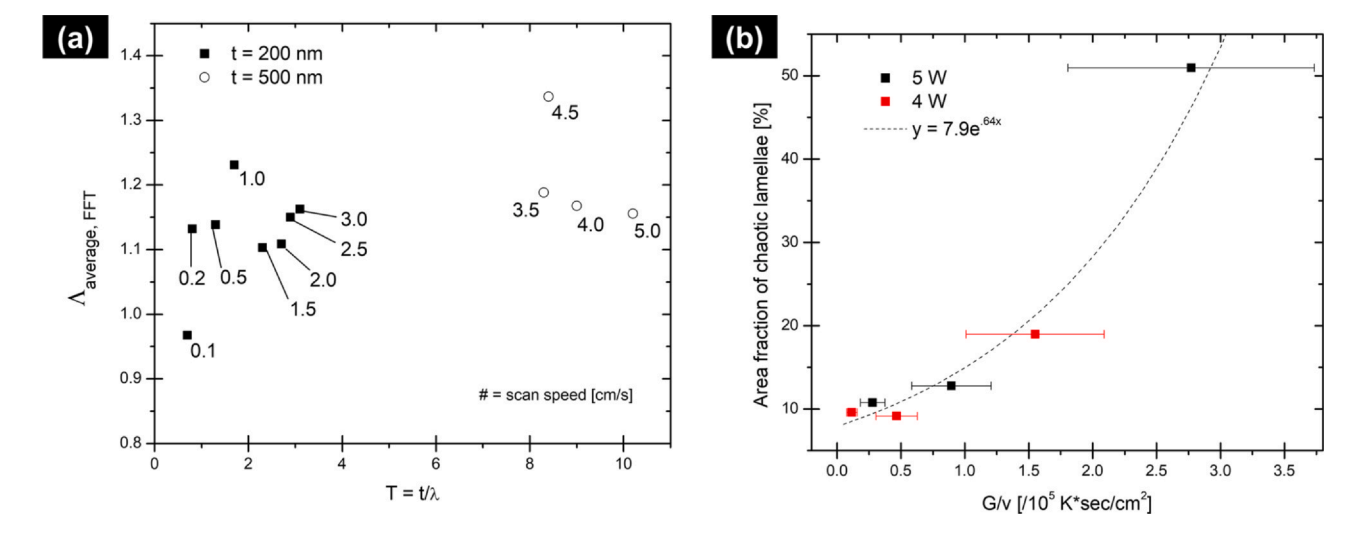


Fig. 10. (a) The average reduced spacing Λ calculated from the FFT as a function of scan speed for eutectic films, where the scan speed is indicated next to each data point. (b) Area fractions of chaotic regions as a function of G/v; data from the 200 nm thick, hypoeutectic film melted at 5 and 4 W.

local lamellar period is known from careful work in the organic eutectics to arise from effects at the boundaries between eutectic grains, and the local variations in $\lambda(y)$ are effectively frozen in along the subsequent length of the melt track. This occurs because so-called phase diffusion, which is the diffusive relaxation of gradients in $\lambda(y)$, is quite sluggish [38].

There is general waviness to the lamellae increasingly observed at higher velocities (see for example, Fig. 5a as compared to Fig. 5c). This is attributed to a decreasing G/v as the scan speed is increased at a constant laser power. A similar result is obtained by decreasing power at constant scan speed, see Fig. S7. This is further supported by a preliminary experiment at v = 3.5 cm/s using a blue laser with a higher power density on a 200 nm near-eutectic film that should provide larger thermal gradients. Lamellae in this case are significantly less wavy, even though the grain size is still relatively small (see Fig. S8).

4.2. Hypoeutectic results

The hypoeutectic films reported here (14–15 at% Cu) all remain in the coupled growth regime across the range of solidification speeds from 0.2 to 1.0 cm/s. As discussed by Jackson and Hunt, coupled growth results from the formation of a compositional boundary layer that allows the solid/liquid interface to attain the eutectic temperature [22]. In steady state, the eutectic lamellae accommodate the deviation from eutectic composition by adjusting the lamellar volume fractions appropriately. However, as discussed by Karma and Sarkissian (K-S), the boundary layer can also play a role in destabilizing the planar eutectic front. Relevant to this, there are four key observations that warrant further discussion here:

- i. The partially melted zone (PMZ) allows us to measure a component of the thermal gradient.
- ii. At the largest speed used here (1.0 cm/s), extensive patches of (primarily) 2λO oscillations and solitary tilt waves are present throughout the melted film. Lamellae are also increasingly wavy with an increase in scan speed, taken to be distinct from the oscillatory instability, similar to observations in eutectic films.
- iii. There is an increasing tendency to form chaotic lamellar structures as G/v *increases*, with a profusion of chaotic structure at 0.2 cm/s.
- iv. In addition to oscillations and solitary tilt waves, tilt patches, hooked lamellae, and extreme lamellar branching were characteristic of the chaotic regions.

(i) The partially melted zone is a natural consequence of melting and resolidification in off-eutectic compositions using a focused heat source, since there must be a region of the thermal profile that never exceeds the liquidus temperature, leading to retention of the primary phase. The thin film geometry presents an advantage over laser melting of bulk specimens with regard to the ease of imaging of the extent and morphology of the solidification microstructure. Note that such a partially melted zone is not observed in steady-state pulling experiments such as those conducted with off-eutectic transparent organics. However, if pulling is stopped, then the primary phase forms in the thermal gradient region where $T_E \leq T \leq T_L$, where $T_{E(L)}$ is the eutectic (liquidus) temperature [23].

The steady-state PMZ width allows us to approximate the thermal gradient, G. Assuming that heat conduction is solely inplane, due to the thermally insulating fused silica substrate, this will provide the value of G in the y direction, denoted here as $G_y = [T_L(C) - T_E]/(PMZ \text{ width})$, where $T_L(C)$ is the liquidus temperature at the hypoeutectic composition, C. As an example, for the film melted at 5 W laser power and 0.2 cm/s scan speed, the mean width of the PMZ is 4.15 μ m. This gives $G_y = 4.6 \pm 1.0 \times 10^6$ K/m, where the uncertainty primarily arises from the estimates on the hypoeutectic composition

as discussed in the Experimental section. Table 1 lists the calculated values for each sample.

G_v is larger for smaller laser scan speeds at constant power, and larger for higher laser powers at constant speed, implying that G_v increases with the peak temperature produced by the laser beam. Note that for an elliptical beam moving along the positive x direction, $G_v \ddagger G_{x-}$, the gradient in the negative x direction along the center of the melt track. The latter quantity is of more interest, since most measurements of the lamellar spacing and morphology are made near track center. Although G_x cannot be determined without detailed modeling of the thermal profile, there will be two competing effects on the magnitude of this component of gradient. Elongation of the elliptical beam along the y direction will tend to make $G_{x-} > G_v$. On the other hand, translation along positive x will tend to reduce G_{x-} . These effects will produce $G_{x-} \ddagger G_{y}$ at most by factors, not by orders of magnitude, hence we will use G_v as a proxy value. While G for eutectic films cannot be measured in the same way, the magnitude must be very close to the hypoeutectic films for the same melting conditions. It is interesting that a 5W laser incident on a thin film supported by a thermally insulating substrate leads to thermal gradients similar to those produced using a kW laser incident on bulk Al-Cu [39].

(ii) At the fastest laser scan speed reported here, 1.0 cm/s, the microstructure is dominated by oscillatory lamellae, wavy lamellae, and solitary tilt waves. In addition to the presence of 2λO oscillatory lamellae, as with the eutectic sample, the increase in velocity at a given laser power yielded wavier lamellae. The presence of the $2\lambda O$ oscillatory mode in hypoeutectic Al-Cu has also been reported by Zimmerman, Karma and Carrard [26]. In both that work and herein, the 2λO oscillations occur only in localized patches, unlike in wellprepared organic films, where regions of 2λO can span hundreds of adjacent lamellae [24]. However, K-S predicts that such behavior will only occur in a narrow range of conditions in the composition/spacing variable space [25]. It becomes easier to destabilize the axisymmetric lamellar state (where "easier" implies that smaller reduced lamellar lengthscales are required) when compositions are further from the eutectic, due to the steeper compositional gradient in the liquid associated with the boundary layer. This composition gradient has a destabilizing effect on the interface akin to constitutional supercooling of a single-phase alloy.

Both Karma [40] and Karma and Sarkissian [25] describe the presence of periodic oscillations as a manifestation of the Mullins-Sekerka (M-S) instability [41], at solidification velocities where the M-S critical wavelength for instability becomes equal to 2λ . An approximation for the critical wavelength is $\lambda_c = 2\pi[D\Gamma/v(T_L-T_E)]^{1/2}$, where Γ is the Gibbs-Thomson capillarity coefficient [42]. Using values appropriate to Al–Cu, $D=2.4\times10^{-9}$ m²/s, $\Gamma=1.5\times10^{-7}$ K-m (mole-weighted average of the values for α and λ [35], v=1 cm/s, $T_L-T_E=20$ K, gives $\lambda_c=267$ nm, whereas $2\lambda=230$ nm was measured for v=1 cm/s (Table 1), which is in reasonable agreement.

The M-S instability approach is often used to describe the transition from planar interface propagation to cellular/dendritic growth, associated with constitutional supercooling of single-phase alloys. As a linear stability theory, it can only describe the earliest stages of growth and should not readily predict the primary arm spacing. An interface instability would typically be expected to exhibit continuous and non-linear amplitude growth around the fastest-growing Fourier component of the interface profile. But K-S showed that in a narrow range of lamellar spacings there can be "limit cycle" behavior that produces temporal periodicity in the interface profile, leading to steady-state formation of extended regions of uniform 2λO oscillatory lamellae having constant oscillation amplitude and longitudinal oscillation period. However, for lamellar spacings that fall above this narrow range, limit cycles are lost, and the interface profile can become unstable, leading to more extreme morphologies, discussed next.

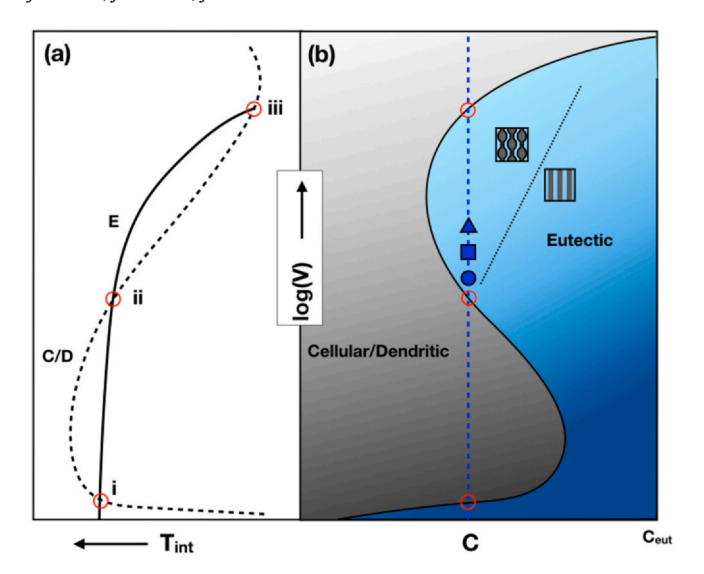


Fig. 11. (a) Schematic plot of the interfacial temperature vs. solidification velocity for eutectic (solid) and cellular/dendritic (dashed) growth. Intersection points (i) – (iii) determine where the competitive growth criterion implies a change in solidification morphology. (b) Schematic representation of the Al–Cu solidification microstructure selection map for hypoeutectic Al–Cu alloys, as developed by Gill et al., here only meant to qualitatively represent boundaries for discussion purposes. Note that the gradients in the color indicate structural lengthscales, where darker is coarser. The three points represent our samples, 1.0 cm/s (triangle), 0.5 cm/s (square) and 0.2 cm/s (circle), all at a single hypoeutectic composition (blue dashed line). Other structural transitions, such as banding, are not shown. Note that the eutectic/cellular boundaries will depend on the actual thermal gradient present in the experiments. In the coupled eutectic region, a transition to oscillatory states is also indicated. (For interpretation of the references to color in this figure legend, the reader is referred to the web version of this article.)

(iii) As shown in Fig. 7, Table 1, and Fig. 10b, there is a profusion of chaotic lamellae that occurs as G/v increases. This is especially true at the scan speed of 0.2 cm/s, where for 5 W laser power, the area fraction of chaotic lamellae more than triples the value measured at 0.5 cm/s. It is usually posited that increasing G/v tends to stabilize interfaces, based on considerations of constitutional supercooling as applied to planar-to-cellular transitions in single-phase alloys. Using the usual criterion of $GD/v > m\Delta C$ for stability, where m is the slope of the liquidus and ΔC is the composition difference from the eutectic, Al-14at%Cu with $G \sim 1 \times 10^6$ K/m (see Table 1) would enter the nominally unstable range for v > 0.01 cm/s. Our experiments are therefore already well into this instability regime. However, calculations of the interface temperatures for cells and for eutectic lamellae in Al-Cu, in the context of the competitive growth criterion [43], yield behavior schematically shown in Fig. 11a. This criterion posits that the morphology with the smallest undercooling, or the highest interfacial temperature T_i, will be preferred. In Fig. 11a, the first crossing point, (i), occurs at very low speeds and corresponds to the interfacial breakdown into cells alluded to above. In Al-Cu, at much higher speeds, there is a second crossover, where the dendrite tip temperature rapidly declines due to capillarity as the tip radii become small. As a result, planar eutectic growth can be re-established. Similar considerations, as a function of alloy composition, underlie the experimentally-determined microstructure selection maps for Al-Cu [39,43]. Fig. 11b shows a portion of the map for Al-Cu, again only schematically. Note the re-entrant eutectic "nose" at higher values of v – the work reported here lies within this region. Hence, we propose that the observation that there is a rapid proliferation of chaotic behavior at 0.2 cm/s arises because we are approaching a eutectic-to-cellular transition from above. The location of the 0.2 cm/s sample at just above the boundary to cellular is quantitatively consistent with the experimental map established for Al-Cu, which puts the transition speed at 0.1 cm/s for a composition

of 14 at% Cu [44]. As discussed by K-S, there is a rich range of unstable behavior possible before the interface fully breaks down into cells or dendrites [25]. It is also important to note that this re-entrant eutectic/cellular transition is present in numerous metallic systems, and at least one ceramic system, so this result may have more general implications [45–50].

Examination of large-area images at v = 0.2 and 0.5 cm/s suggest that chaotic regions are likely to be associated with specific eutectic grains (see Figs. S4 and S5). The grain boundaries provide sources of solitary tilt waves, as noted, for example, in Ref. [29], but do not appear to be inherently responsible for the chaos itself, as the grain size increases rapidly as v decreases. It is acknowledged, however, that it was not established whether the grain size normalized by the lamellar period also decreases with decreasing v. We hypothesize that certain grains contain larger locked-in lamellar periods determined at their nucleation stage (larger Λ), and these grains are most susceptible to chaotic interface fluctuations [38]. Given the large angles, and continuous curvatures of lamellae in the chaotic regions, crystallographic anisotropy is not thought to play a determining role in fostering chaotic behavior, that is, all grains are of the "floating" type [24].

(iv). The morphologies that form in the chaotic regions may lend some insights into the potential breakdown of the interface as velocity is reduced towards the cellular transition. In addition to $2\lambda O$ oscillations, extended tilt waves, hook-shaped lamellae, and extreme lamellar branching (ELB) are frequent components. Extended tilt waves have larger widths and often cluster, produced larger regions of tilt, albeit still smaller than those observed in well-conditioned organic films, and the tilted lamellae are usually also undergoing some form of oscillatory behavior as well. Stable regions of pure tilt were not observed, in agreement with K-S predictions that for phase diagrams with symmetric eutectic regions, tilt can occur at large enough $\Lambda(C)$, but the tilted lamellae are susceptible to perturbations that will render them unstable across the entire parameter space.

Hook-shaped lamellae are shown in Fig. 8a and 8b, and in close inspection of Fig. 7a. These have been predicted by Karma and Sarkissian as manifestations of instability occurring at large Λ . In their modeling, the hooks result from large-amplitude oscillations superimposed on tilted lamellae, leading to lamellar collisions, and the hook itself always forms on the same side of the minority-phase lamellae, presumably due to the symmetry breaking associated with tilt. In our films, the hooks are often <u>not</u> associated with local tilt, and as such the hooks frequently form on alternating sides of the minority-phase (θ) lamellae.

Extreme lamellar branching appears to be a new morphology, although structures with a somewhat similar appearance were reported by Akamatsu, et al. as "giant transitory oscillations" [23]. A branching event occurs when a primary-phase (α) lamellae suddenly coarsens significantly and then splits in two, and the resulting branches diverge from one another at angles that can approach 90°. The branches do not outrun the surrounding lamellae and the coupled α/θ growth can recover as the branches reconverge. In the region between the branches, a fine-scale lamellar region forms that resembles an interdendritic eutectic. This eutectic is occasionally observed to propagate in a direction almost normal to the local propagation of the macroscopic L/S interface. These observations lend some credence to the connection of chaotic lamellae to the reentrant cellular-eutectic transition. Exactly how the ELB event evolves in not known. It may form at a crossing point between two extended tilt waves. The inset in Fig. 8b depicts a condition where two smaller tilt waves cross, and the intersection produces a feature that is similar to, but smaller than, an ELB event. These events also occur frequently in the center of the melt track, i.e. where many tilt waves converge.

In all the hypoeutectic melt tracks, we observed slight laser power variations. For example, the width of the melt track for the 5~W, 1.0~cm/s scan oscillated between $172~and~175~\mu m$ every 8~ms. By comparing the different track widths for the 5~W and 4~W experiments, we calibrated how the track width varies with laser power, which was found to vary by about $\pm~1\%$. This small variation in power was briefly considered as a cause for the chaotic lamellae found in the hypoeutectic samples, but it was eliminated as a possibility as ELB events were found to occur on a smaller timescale than the power fluctuations.

4.3. Improving laser directional solidification experiments in thin films

The results here represent the complex solidification behavior that arises from a laser beam scanning across a continuous thin film. Laser melting has an inherent advantage of being relatively easy to set up and carry out. However, as should be clear by now, laser melting of films is currently much less refined relative to the types of experimental setups and degree of control that have been developed for transparent organic eutectics. To simplify and better understand the solidification behavior of hypoeutectic thin metal films at these velocities, particularly at steady state, three aspects of the methodology could be improved. The first improvement relates to the heat loss to the adjacent unmelted film, which results in curved lamellae that converge near the center of the melt track. Instead of melting a track within a continuous film on the substrate, lithography or masking could be used to create film stripes with widths smaller than the laser beam's diameter. Heat can then only be removed antiparallel to the scan direction, which should result in parallel lamellae across the entire track. The second area of improvement relates to the uncontrolled nucleation of eutectic grains, and the difficulty in assuring true steady state solidification conditions. Especially in the hypoeutectic sample, there are no consistent central lamellae; grains continuously nucleate on the sides of the PMZ and then eventually converge in the center of the track, pinching off other grains (refer to Fig. S9). As a result, although micrographs are taken several millimeters beyond where the laser melt track initiates, the lamellae observed may only ever be a few hundred microns from their nucleation site at the track edge. Consequently, we cannot consider our results as an outcome of true steady state growth. This could potentially be solved with a further modification to a deposition mask where a constriction near the beginning of the strip could emulate a single grain selector, akin to that in Ref. [51], to permit only the growth of a single eutectic grain. The third means to improve laser-based directional solidification of thin films relates to the laser fluence, where fluence (the optical energy per area) depends on both laser power and scan speed. Comparisons of solidification morphology at different scan speeds should be done at constant fluence. For example, if the fluence were to be held constant across all solidification velocities, it is expected that the waviness, found at higher velocities due to a lower G/v could be mitigated, see Fig. S8. If the effective fluence is kept constant, the maximum temperature and approximate values of G/v should remain consistent. This requires a larger dynamic range of laser powers, which should scale with the range of scan speeds of interest to the experimentalist. These modifications would improve thin film laser solidification experiments for scientific investigation of solidification morphologies where the growth conditions could truly attain steady state, with controlled G, and provide results that are not muddled by potential grain boundary effects.

5. Conclusions

Directional solidification by laser scanning of eutectic and hypoeutectic Al–Cu alloys films as thin as 200 nm was investigated. For eutectic films, well-ordered lamellae are obtained at lower velocities, but with increasing velocity (at constant laser power) the

lamellar regularity decreases. Small grains and lamellar waviness are correlated with decreasing G/v. Overall, films of 200 and 500 nm thickness (and thicker films from the literature) were found to obey the relationship $\lambda^2 v = K$, where the measured K for films is larger than both the commonly accepted values obtained in bulk and the expected theoretical value. This is thought to be related to the larger distribution of lamellar spacings built into the eutectic grains and inherent limitations on self-regulation of the long-period modes in 2D systems vis-à-vis bulk. Directional solidification of hypoeutectic Al-Cu films produced a partially melted zone along the track boundaries, and between these zones, a fully melted region where lamellar instabilities were evident. In the regime of solidification velocity studied here, chaotic lamellar instabilities became more prevalent as G/v increased. This is attributed to the melts being within a re-entrant eutectic region of the microstructure selection map, wherein decreasing v approaches a cellular/dendritic transition from above. Extreme lamellar branching events were a key characteristic of the chaotic regions and may presage how the transition to cellular/dendritic morphologies would occur at even lower speeds. Finally, we have suggested improvements to laser directional solidification experiments in thin films that permit better control over the power inputs, heat flow, and grain size.

CRediT authorship contribution statement

E. J. Sullivan: Investigation, Data curation, Formal analysis, Visualization, Writing - original draft, Writing - review & editing. J. A. Tomko: Investigation, Data curation, Writing - review & editing. J. M. Skelton: Investigation, Writing - review & editing. J. M. Fitz-Gerald: Funding acquisition, Supervision, Writing - review & editing. P. E. Hopkins: Funding acquisition, Supervision, Writing - review & editing. J. A. Floro: Conceptualization, Formal analysis, Visualization, Funding acquisition, Supervision, Writing - original draft, Writing - review & editing, Project administration.

Declaration of Competing Interest

The authors declare that they have no known competing financial interests or personal relationships that could have appeared to influence the work reported in this paper.

Acknowledgements

Support from the National Science Foundation under grant number DMR #1663085 and the Office of Naval Research under grant number N00014-15-1-2769 is gratefully acknowledged. Thanks to Jim Howe for useful conversations, to Helge Heinrich for help with FIB work, and to Steve Rossnagel for advice and for help with the film growth.

Appendix A. Supporting information

Supplementary data associated with this article can be found in the online version at doi:10.1016/j.jallcom.2021.158800.

References

- [1] M. Zimmermann, M. Carrard, W. Kurz, Rapid solidification of Al-Cu eutectic alloy by laser remelting, Acta Met. 37 (1989) 3305–3313, https://doi.org/10.1016/ 0001-6160(89)90203-4
- [2] Trepczynska Lent, Rod and lamellar growth of eutectic, Arch. Foundry Eng. 10 (2010) 179–184 (http://www.afe.polsl.pl/index.php/pl/296/rod-and-lamellar-growth-of-eutectic.pdf).
- [3] S. Pauly, P. Wang, U. Kühn, K. Kosiba, Experimental determination of cooling rates in selectively laser-melted eutectic Al-33Cu, Addit. Manuf. 22 (2018) 753-757, https://doi.org/10.1016/j.addma.2018.05.034
- [4] X.P. Li, X.J. Wang, M. Saunders, A. Suvorova, L.C. Zhang, Y.J. Liu, M.H. Fang, Z.H. Huang, T.B. Sercombe, A selective laser melting and solution heat treatment

- refined Al-12Si alloy with a controllable ultrafine eutectic microstructure and 25% tensile ductility, Acta Mater. 95 (2015) 74-82, https://doi.org/10.1016/j.actamat 2015 05 017
- [5] W.A. Jensen, N. Liu, B.F. Donovan, J.A. Tomko, P.E. Hopkins, J.A. Floro, Synthesis and thermal transport of eco-friendly Fe-Si-Ge alloys with eutectic/eutectoid microstructure, Mater. Chem. Phys. 207 (2018) 67–75, https://doi.org/10.1016/j. matchemphys 201712 038
- [6] T. Ikeda, L.A. Collins, V.A. Ravi, F.S. Gascoin, S.M. Haile, G.J. Snyder, Self-assembled nanometer lamellae of thermoelectric PbTe and Sb 2 Te 3 with epitaxy-like Interfaces, Chem. Mater. 19 (2007) 763–767, https://doi.org/10.1021/cm062121p
- [7] E.F. Kneller, R. Hawig, The exchange-spring magnet: a new material principle for permanent magnets, IEEE Trans. Magn. 27 (1991) 3560–3588, https://doi.org/10. 1109/20102931
- [8] B. Chanda, G. Potnis, P.P. Jana, J. Das, A review on nano-/ultrafine advanced eutertic alloys, J. Alloy. Compd. 827 (2020) 154226, https://doi.org/10.1016/j.ipllcom/2020154226
- [9] H.E. Cline, Directionally solidified thin-film eutectic alloys, J. Appl. Phys. 52 (1981) 256–260. https://doi.org/10.1063/1.328485
- [10] B.M. Ditchek, Periodic Si-CoSi2 eutectic structures, J. Appl. Phys. 61 (1987) 5419–5424, https://doi.org/10.1063/1.338282
- [11] J. Kim, Y. Jung, S. Lee, S. Hong, S. Choi, J. Kim, T. Park, E. Lee, J.Y. Won, H.I. Lee, Y.J. Lee, B. Kim, J.J. Kim, Y. Kim, K. Hwang, C.W. Yang, H. Kim, Lamellar-structured Ni-silicide film formed by eutectic solidification, J. Alloy. Compd. 771 (2019) 124–130, https://doi.org/10.1016/j.jallcom.2018.08.257
- [12] S. Akamatsu, S. Bottin-Rousseau, G. Faivre, Determination of the Jackson-Hunt constants of the In-In2Bi eutectic alloy based on in situ observation of its solidification dynamics, Acta Mater. 59 (2011) 7586–7591, https://doi.org/10.1016/j. actamat.2011.08.036
- [13] H.E. Cline, Growth of eutectic alloy thin films, Mater. Sci. Eng. 65 (1984) 93–100, https://doi.org/10.1016/0025-5416(84)90203-9
- [14] G.A. Chadwick, Solidification of CuAl2-Al eutectic alloys, J. Inst. Met. 19 (1963)
- [15] J.D. Livingston, H.E. Cline, E.F. Koch, R.R. Russell, High-speed solidification of several eutectic alloys, Acta Met. 18 (1970) 399–404, https://doi.org/10.1016/ 0001-6160(70)90125-2
- [16] A. Moore, R. Elliott, The solidification of metals, ISI 110 (1968) 167.
- [17] M.H. Burden, H. Jones, Determination of cooling rate in splat-cooling from scale of microstructure. J. Inst. Met. 98 (1970) 249–252.
- [18] J.N. Clark, R. Elliott, Interlamellar spacing measurements in the Sn-Pb and Al-CuAl2 eutectic systems, Metall. Trans. A. 7 (1976) 1197–1202, https://doi.org/10. 1007/RF02656603
- [19] J.H. Lee, S. Liu, R. Trivedi, The effect of fluid flow on eutectic growth, Metall. Mater. Trans. A 36 (2005) 3111–3125, https://doi.org/10.1007/s11661-005-0083-6
- [20] D.J.S. Cooksey, D. Munson, M.P. Wilkinson, A. Hellawell, The freezing of some continuous binary eutectic mixtures, Philos. Mag. 10 (1964) 745–769, https://doi. org/10.1080/14786436408225381
- [21] A. Ourdjini, J. Liu, R. Elliott, Eutectic spacing selection in Al-Cu system, Mater. Sci. Technol. 10 (1994) 312–318, https://doi.org/10.1179/mst.1994.10.4.312
- [22] K.A. Jackson, J.D. Hunt, Binary eutectic solidification, Transactions of the Metallurgical Society, Elsevier, AIME, 1966, pp. 843–852.
- [23] S. Akamatsu, S. Bottin-Rousseau, M. Perrut, G. Faivre, V.T. Witusiewicz, L. Sturz, Real-time study of thin and bulk eutectic growth in succinonitrile-(d)camphor alloys, J. Cryst. Growth 299 (2007) 418–428, https://doi.org/10.1016/j.jcrysgro. 2006.11.271
- [24] M. Ginibre, S. Akamatsu, G. Faivre, Experimental determination of the stability diagram of a lamellar eutectic growth front, Phys. Rev. E 56 (1997) 780-796, https://doi.org/10.1103/PhysRevE.56.780
- [25] A. Karma, A. Sarkissian, Morphological instabilities of lamellar eutectics, Metall. Mater. Trans. A Phys. Metall. Mater. Sci. 27 (1996) 635–656, https://doi.org/10. 1007/BF02648952
- [26] M. Zimmermann, A. Karma, M. Carrard, Oscillatory lamellar microstructure in off-eutectic Al-Cu alloys, Phys. Rev. B 42 (1990) 833–837, https://doi.org/10.1103/ Phys. Rev. B 42 (1990) 833–837, https://doi.org/10.1103/
- [27] J.L. Braun, C.J. Szwejkowski, A. Giri, P.E. Hopkins, On the steady-state temperature rise during laser heating of multilayer thin films in optical pump-probe techniques, J. Heat. Transf. 140 (2018) 1–10, https://doi.org/10.1115/1.4038713
- [28] J.A. Tomko, D.H. Olson, J.L. Braun, A.P. Kelliher, B. Kaehr, P.E. Hopkins, Substrate thermal conductivity controls the ability to manufacture microstructures via

- laser-induced direct write, Appl. Phys. Lett. 112 (2018) 051906, https://doi.org/10.1063/1.5016073
- [29] G. Faivre, J. Mergy, Tilt bifurcation and dynamical selection by tilt domains in thin-film lamellar eutectic growth: experimental evidence of a tilt bifurcation, Phys. Rev. A. 45 (1992) 7320–7329, https://doi.org/10.1103/PhysRevA.45.7320
- [30] R. Trivedi, P. Magnin, W. Kurz, Theory of eutectic growth under rapid solidification conditions, Acta Met. 35 (1987) 971–980, https://doi.org/10.1016/0001-6160(87)90176-3
- [31] O. Senninger, M. Peters, P.W. Voorhees, Two-phase eutectic growth in Al-Cu and Al-Cu-Ag, Metall. Mater. Trans. A 49 (2018) 1692–1707, https://doi.org/10.1007/ s11661-018-4488-4
- [32] J. Sun, S.L. Simon, The melting behavior of aluminum nanoparticles, Thermochim. Acta 463 (2007) 32–40, https://doi.org/10.1016/j.tca.2007.07.007
- [33] M. Tassa, J.D. Hunt, The measurement of Al-Cu dendrite tip and eutectic interface temperatures and their use for predicting the extent of the eutectic range, J. Cryst. Growth 34 (1976) 38–48, https://doi.org/10.1016/0022-0248(76)90260-8
- [34] V.T. Witusiewicz, U. Hecht, S. Rex, In-situ observation of eutectic growth in Albased alloys by light microscopy, J. Cryst. Growth 372 (2013) 57–64, https://doi. org/10.1016/j.jcrysgro.2013.02.033
- [35] H. Walker, S. Liu, J.H. Lee, R. Trivedi, Eutectic growth in three dimensions, Metall. Mater. Trans. A Phys. Metall. Mater. Sci. 38 A (2007) 1417–1425, https://doi.org/ 10.1007/s11661-007-9163-0
- [36] K. Kassner, C. Misbah, R. Baumann, Eutectic dynamics: a host of new states, Phys. Rev. E 51 (1995) 2751–2754, https://doi.org/10.1103/PhysRevE.51.R2751
- [37] R. Trivedi, J.T. Mason, J.D. Verhoeven, W. Kurz, Eutectic spacing selection in lead-based alloy systems, Metall. Trans. A 22 (1991) 2523–2533, https://doi.org/10.1007/BF02665018
- [38] B. Caroli, C. Caroli, G. Faivre, J. Mergy, Lamellar eutectic growth of CBr4-C2C16: effect of crystal anisotropy on lamellar orientations and wavelength dispersion, J. Cryst. Growth 118 (1992) 135–150, https://doi.org/10.1016/0022-0248(92) 90058
- [39] S.C. Gill, W. Kurz, Rapidly solidified AlCu alloys-I. experimental determination of the microstructure selection map, Acta Metall. Mater. 41 (1993) 3563–3573, https://doi.org/10.1016/0956-7151(93)90237-M
- [40] A. Karma, Beyond steady-state lamellar eutectic growth, Phys. Rev. Lett. 59 (1987) 71–74, https://doi.org/10.1103/PhysRevLett.59.71
- [41] W.W. Mullins, R.F. Sekerka, Stability of a planar interface during solidification of a dilute binary alloy, J. Appl. Phys. 35 (1964) 444–451, https://doi.org/10.1063/1. 17(2222)
- [42] W. Kurz, D.J. Fisher, Dendrite growth in eutectic alloys: the coupled zone, Int. Mater. Rev. 24 (2012) 177–204, https://doi.org/10.1179/095066079790136408
- [43] S.C. Gill, W. Kurz, Rapidly solidified Al-Cu alloys—II. Calculation of the microstructure selection map, Acta Metall. Mater. 43 (1995) 139–151, https://doi.org/ 10.1016/0956-7151(95)90269-4
- [44] S.C. Gill, M. Zimmermann, W. Kurz, Laser resolidification of the AlAl2Cu eutectic: the coupled zone, Acta Metall. Mater. 40 (1992) 2895–2906, https://doi.org/10. 1016/0956-7151(92)90454-M
- [45] S. Fukumoto, W. Kurz, Solidification phase and microstructure selection maps for Fe-Cr-Ni alloys, ISIJ Int 39 (1999) 1270–1279, https://doi.org/10.2355/ isijinternational.39.1270
- [46] P. Gilgien, A. Zryd, W. Kurz, Metastable phase diagrams and rapid solidification processing, ISIJ Int. 35 (1995) 566–573, https://doi.org/10.2355/isijinternational. 25,566
- [47] A. Hawksworth, W.M. Rainforth, H. Jones, Solidification microstructure selection in the Al-rich Al-La, Al-Ce and Al-Nd systems, J. Cryst. Growth 197 (1999) 286–296, https://doi.org/10.1016/S0022-0248(98)00955-5
- [48] P. Mohammadpour, A. Plotkowski, A.B. Phillion, Revisiting solidification microstructure selection maps in the frame of additive manufacturing, Addit. Manuf. 31 (2020) 100936, https://doi.org/10.1016/j.addma.2019.100936
- [49] S. Bourban, N. Karapatis, H. Hofmann, W. Kurz, Solidification microstructure of laser remelted Al203-ZrO2 eutectic, Acta Mater. 45 (1997) 5069–5075, https:// doi.org/10.1016/S1350-6454(07)00108-5
- [50] P. Gilgien, A. Zryd, W. Kurz, Microstructure selection maps for Al-Fe alloys, Acta Metall. Mater. 43 (1995) 3477–3487, https://doi.org/10.1016/0956-7151(95) 00020 Y
- [51] S. Bottin-Rousseau, M. Perrut, C. Picard, S. Akamatsu, G. Faivre, An experimental method for the in situ observation of eutectic growth patterns in bulk samples of transparent alloys, J. Cryst. Growth 306 (2007) 465–472, https://doi.org/10.1016/ j.jcrysgro.2007.05.035